

PAPER

# Laser polarization driven micromanipulation and reorientation dynamics of an asymmetric shaped microscopic biomaterial using optical tweezers

To cite this article: Chetana D *et al* 2022 *J. Opt.* **24** 094007

View the [article online](#) for updates and enhancements.

## You may also like

- [New Constraints on Pluto's Sputnik Planitia Ice Sheet from a Coupled Reorientation–Climate Model](#)  
Perianne E. Johnson, James T. Keane, Leslie A. Young et al.
- [Temperature–pressure-induced solid–solid 100 to 110 reorientation in FCC metallic nanowire: a molecular dynamic study](#)  
Vijay Kumar Sutrakar, D Roy Mahapatra and A C R Pillai
- [Deciphering the Morphological Origins of X-shaped Radio Galaxies: Numerical Modeling of Backflow versus Jet Reorientation](#)  
Gourab Giri, Bhargav Vaidya and Christian Fendt

# Laser polarization driven micromanipulation and reorientation dynamics of an asymmetric shaped microscopic biomaterial using optical tweezers

Chetana D<sup>1</sup> , Praveen P<sup>1,2</sup>, Nagesh B V<sup>3</sup>, Sarbari Bhattacharya<sup>1</sup> and Sharath Ananthamurthy<sup>4,\*</sup> 

<sup>1</sup> Department of Physics, Jnanabharathi Campus, Bangalore University, Bengaluru 560056, India

<sup>2</sup> Chemical and Process Engineering, University of Strathclyde, 75 Montrose Street, Glasgow G11XL, United Kingdom

<sup>3</sup> Department of Physics, M S Ramaiah Institute of Technology, MSR Nagar, MSRIT Post, Bangalore 560054, India

<sup>4</sup> School of Physics, University of Hyderabad, Hyderabad 500046, India

E-mail: [sasp@uohyd.ac.in](mailto:sasp@uohyd.ac.in)

Received 17 October 2021, revised 18 July 2022

Accepted for publication 3 August 2022

Published 17 August 2022



## Abstract

We present measurements and a theoretical model that describes the dynamics of ellipsoidal shaped, chicken red blood cells (cRBCs) reorienting in an optical trap and demonstrates the ability to control their reorientation through changes in the intensity distribution that results from the different states of the polarization of the trapping laser. We have observed that in linearly polarized light, cRBC, a type of avian RBC, undergoes dual reorientation, with the first reorientation about the cell's major axis and the second, about its short minor axis, with the major axis aligning with the laser propagation direction at equilibrium. We compute the work done for each of these reorientations and attribute the observed dynamics to a minimization of the energy cost for the particular sequence of the reorientations that we observe. Further, we achieve a controlled second orientation of the major axis along the laser propagation direction by varying the ellipticity of the polarization of the laser. We explain these partial second reorientation results by employing a geometrical optics-based model. Characterizing the dynamics and control of these regular-shaped natural soft materials through optical polarization is relevant in the context of current work in the design and development of microscopic artefacts such as lab-on-a-chip platforms.

Supplementary material for this article is available [online](#)

Keywords: optical tweezers, red blood cells, polarization, reorientation

(Some figures may appear in colour only in the online journal)

\* Author to whom any correspondence should be addressed.

## 1. Introduction

Any asymmetric microstructure acquires an equilibrium orientation in an optical trap (OT) in a way so as to maximize the volume in interaction with the region of the greatest electric field [1]. Thus, a biconcave-shaped human red blood cell (hRBC) orients edge-on or flat about the laser propagation direction depending on it being a Gaussian beam trap or Laguerre–Gaussian beam (LG beam) trap of high topological charge, respectively [2]. In the work of Gupta *et al* [2], the tilt of the trapped hRBC is controlled by varying the topological charge of the trapping LG beam. Among other microscopic shapes that have been carefully studied to determine the final equilibrium orientation, is that of a cylinder. Gauthier *et al* [3, 4] have studied the effects of both length and aspect ratio on the orientation of microcylinders in an OT. In the Rayleigh regime, Cao *et al* [5] have shown through simulations, that a trapped cylinder orients edge-on in circularly polarized light and gets pinned to the electric-field direction in linearly polarized light. Further complexity to this problem is introduced when the trapped asymmetric microstructure possesses birefringence. It was shown in [1] that while the non-birefringent discs show rotational diffusion after acquiring an edge-on orientation, the birefringent discs show rotation along with the changing direction of linear polarization due to a birefringence induced torque.

While previous work has mostly concentrated on studying the effects of size and shapes on reorientation dynamics [4, 5] or by altering the technique of trapping the object [6–11], in this work we study the influence of the polarization of the laser on the trapping dynamics of chicken red blood cells (cRBCs), a weakly birefringent asymmetric microstructure.

The dimensions of a cRBC, a triaxial structure, (figure 1), are about  $12\ \mu\text{m}$  along the major axis,  $7\ \mu\text{m}$  along the long minor axis, and  $4\ \mu\text{m}$  along the short minor axis [12]. The unique shape of cRBC makes it an interesting choice to study the interplay between the drag-torques, shape-asymmetry-induced torques, and laser-induced torques in determining the trapping dynamics.

### 1.1. Sample preparation

The blood sample of a healthy chicken is taken out of the vein from one of its wings and mixed with equal amounts of normal saline solution and centrifuged thrice at a rate of 1500–2000 rpm. The blood obtained thus, is stored with an equal amount of normal saline solution and maintained at  $4^\circ\text{C}$ . About  $10\ \mu\text{l}$  of this solution is taken in about 2 ml of normal saline. This solution is further diluted by taking  $5\ \mu\text{l}$  of this solution with  $400\ \mu\text{l}$  of normal saline in a cavity formed by an O-ring of diameter 1 cm and thickness of 1 mm which is stuck on a coverslip. The solution in the ring is overfilled with normal saline and then covered with another glass slide to seal the entire solution in place. Experiments were performed at room temperature within 4 hours of adding the sample to the O-ring cavity.

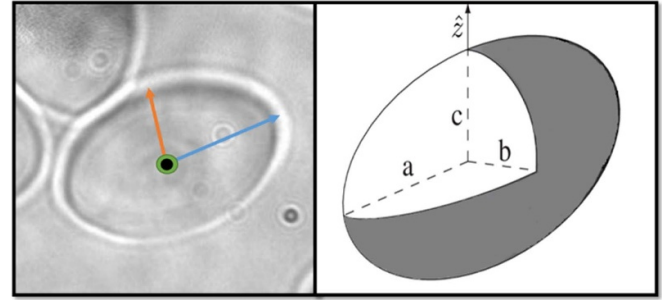


**Figure 1.** (a) Image of cRBC with major axis (in blue) and first minor axis (in orange) viewed in the XY plane. The black marker indicates the second minor axis that is along the laser propagation direction (perpendicular to the image). (b) Schematic of cRBC as a triaxial ellipsoid with major (a) and two minor ((b) and (c)) axes.

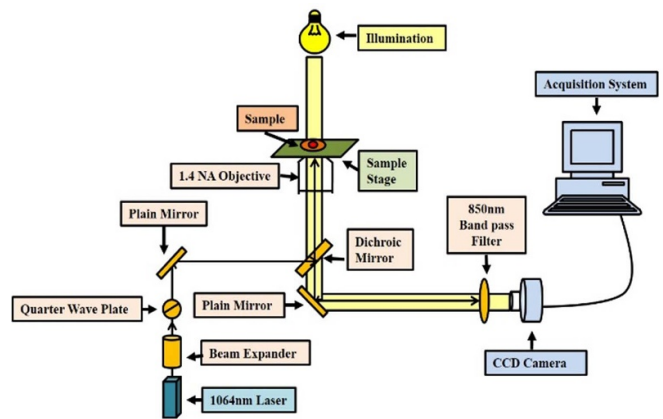


**Figure 2.** Schematic of the optical tweezer setup used in our study.

### 1.2. Experimental setup

The experimental setup is described elsewhere [13] and the schematic of the same is shown in figure 2. A single beam optical tweezer setup is built around an inverted microscope (IX71, Olympus). This consists of a Ytterbium fibre laser of wavelength 1064 nm, a wavelength used often for biological samples to avoid damage due to laser absorption. The quarter-wave plate (QWP) introduced in the path of the laser beam is to change the ellipticity of the polarization. This beam passes through a beam expander to overfill the aperture of a  $100\times$  high numerical aperture (NA) objective (Olympus uPlan FI 100 $\times$ , oil immersion, NA = 1.4, working distance (WD) = 0.17 mm) which focuses the laser beam. The cRBC sample is placed in a sample holder mounted on a nanometer precision three-axis (XYZ) piezoelectric transducer stage. There is a provision for video imaging by a charge-coupled device (CCD) camera. The entire setup is on a vibration isolation table (TMC, USA). All optics used here are from Thorlabs, USA, while the Optomechanical components are from Holmarc, India.

The field of view of the camera is found to be  $72\ \mu\text{m}$ – $86\ \mu\text{m}$ . The concentration of the cRBCs in the solution prepared was adjusted so that there were three to four cells in each image. The orientation of the slow axis of the QWP is changed gradually for each measurement before trapping

to observe and record the resultant dynamics. The recorded images are analysed using ImageJ software.

## 2. Results and discussions

Experiments are performed using the blood sample collected from three different specimens of *Gallus domesticus* which were monitored regularly for their health condition to ensure minimal variation in the blood drawn from them. All the cRBCs are trapped at a sufficient distance away from the coverslip to ensure minimal disturbance from any hydrodynamic effects, due to the presence of the latter [14–16]. Each blood sample is used to perform the experiments at three different laser powers of 4.86 mW, 7.55 mW, and 10.27 mW. The slow axis of the QWP is aligned along the linear polarization direction of the laser beam. For each value of power at the sample stage, the slow axis of the QWP is varied in the steps of  $5^\circ$  and the response is recorded for all these angles of the QWP along with the angles for obtaining circularly polarized light (i.e.  $45^\circ$ ,  $135^\circ$ ,  $225^\circ$  and  $315^\circ$ ). About 200 trials are recorded for each setting of the QWP and the results are analysed. The error bars have been computed by calculating the standard deviation over these trails subjected to identical torques.

### 2.1. Reorientation dynamics in linearly polarized light

In contrast to previous work addressing orientation measurements where only a single orientation is observed for an asymmetric object [1–11, 17], in these experiments we observe two distinct orientations of cRBC before it reaches a final equilibrium orientation. The dynamics of the cRBC under the influence of linearly polarized light in an OT is shown in figure 3. We observe that the cell undergoes dual-orientation with its first orientation about the major axis as shown in figures 3(A)–(C) and the second, about the short minor axis as shown in figures 3(D)–(F), to maximize its volume along the region of the highest electric field. In doing so, it attains a stable final orientation about the laser propagation direction. Previous work [18] has shown that the hRBC undergoes folding when trapped in optical tweezers. However, our calculations, presented in appendix A, establish that the energy required for folding or even deforming the cRBC is far greater than that required for reorienting the cell. Calculations about cell reorientation are shown below.

We explain the observed dual reorientation behaviour by considering the interplay between rotational drag for reorientation,  $\tau_{\text{drag}}$ , about different axes of cRBC, and the corresponding laser-induced torques  $\tau_{\text{laser}}$ . The schematic for the same is described in figure 4. The first orientation is about the major axis which we call *Reorientation A*, and the second orientation is about the short minor axis of the cell and is called *Reorientation B*. We also consider a direct orientation about the long minor axis of the ellipsoid, called *Reorientation C*, in our calculations. As it is experimentally observed that we see the cell undergo a combination of *Reorientation A* followed by *Reorientation B* instead of a direct reorientation, i.e. *Reorientation C*, it is important to understand why this is so.

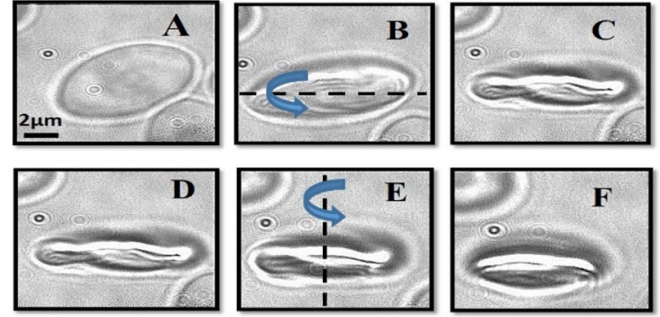


**Figure 3.** (A) cRBC reorienting about the major axis as in figures (A)–(C). The cRBC in figure continues to show further reorientation, this time, about an axis perpendicular to the plane of the cRBC, as seen from figures (D)–(F).

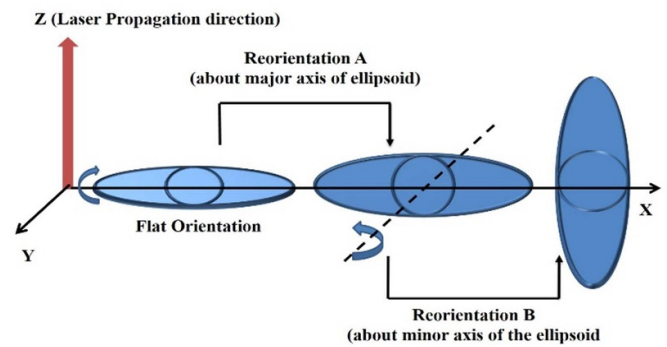


**Figure 4.** Schematic depicting the dual orientations of the cRBCs where the first orientation is about the major axis ( $x$ -axis) and the second orientation is about the minor axis ( $y$ -axis). The circle shown is to help provide a perspective.

The process of reorientation of the cRBC in the OT can be understood with the help of the rotational Langevin equation:

$$\tau_{\text{inertia}} + \tau_{\text{drag}} = \tau_{\text{laser}} + \tau_{\text{thermal}}. \quad (1)$$

The corresponding inertial torques ( $\tau_{\text{inertia}}$ ) about the three axes are estimated and found to be four orders of magnitude smaller than the laser torque (appendix B). The torques introduced due to thermal forces ( $\tau_{\text{thermal}}$ ) are random and therefore cancel out during the reorientation. Ignoring,  $\tau_{\text{inertia}}$  and  $\tau_{\text{thermal}}$ , we get

$$\tau_{\text{laser}} = \tau_{\text{drag}}. \quad (2)$$

This implies that the torque induced due to the laser on the cRBC ( $\tau_{\text{laser}}$ ) is utilized by the cell to overcome the drag torque ( $\tau_{\text{drag}}$ ) in its reorientation. We name the axis about which the reorientation of the cRBC happens as  $\text{Axis}_{\text{reorient}}$ . Taking  $\epsilon$  to be the angle subtended by the axis perpendicular to  $\text{Axis}_{\text{reorient}}$  with the plane containing  $\text{Axis}_{\text{reorient}}$ , we can write the general equation for the work done in a complete reorientation process of a cRBC as

$$W = \int_0^{\pi/2} \tau_{\text{drag}} d\epsilon \quad (3)$$

**Table 1.** Summary of calculations involving laser-induced torques, rotational drag coefficients, and the corresponding work done for the three orientations described.

	Reorientation A	Reorientation B	Reorientation C
$\gamma$ (Nms rad <sup>-1</sup> )	$1.61 \times 10^{-18}$	$1.40 \times 10^{-18}$	$3.02 \times 10^{-18}$
Work done (J)	$1.80 \times 10^{-18}$	$1.57 \times 10^{-18}$	$3.39 \times 10^{-18}$

where  $\tau_{\text{drag}} = \gamma \dot{\epsilon}$  and  $\gamma$  is the rotational drag coefficient of the cell which depends on the orientation it takes with respect to the laser propagation direction, and  $\dot{\epsilon}$  is the first-order derivative of the angular displacement  $\epsilon$ , with respect to time. To estimate the work done we approximate the shape of cRBC to that of an ellipsoid.

From [19], the drag coefficient for reorientation about the major axis is given by

$$\gamma = \frac{16}{3} \pi \eta a b^2 \quad (4)$$

and that for reorientation about the minor axis is given by

$$\gamma = \frac{\frac{8}{3} \pi \eta a^3}{\ln \frac{2a}{b} - \frac{1}{2}} \quad (5)$$

where  $\eta$  is the dynamic viscosity of the medium of suspension and  $a$  and  $b$  are the major and minor axes of the ellipsoid, respectively. The drag coefficients in the reorientations A, B and C are different as the rotations are with respect to the different axes of the ellipsoidal body. The work done for the three orientation processes is computed and summarized in Table 1.

From table 1 we find that the work done in each of the steps, Reorientation A and B, is lower when compared to that in Reorientations C. Therefore, the cRBC will first reorient about the major axis i.e. it undergoes Reorientation A. Further, Reorientation B follows to maximize the cell's volume in the region of the highest electric field. As Reorientation C is energetically unfavourable compared to the other reorientations, this is not observed experimentally.

## 2.2. Reorientation dynamics of the second orientation and influence of the polarization of light

The use of elliptically polarized light leads to interesting dynamics. The first reorientation completes the 90° flip the same way as observed when using linearly polarized light, but now the extent of the second reorientation shows a strong dependence on the ellipticity of the polarization. Changing the ellipticity of the beam results in partial second reorientation and we observe that the major axis of cRBC now makes an angle with respect to the laser beam direction. The partial second reorientation varies proportionally with the increase in the ellipticity of the polarization.

We show in figures 5(A)–(E), that the images of cRBC formed at the focal plane after attaining the final equilibrium position after the second reorientation about the minor axis, as the angle of the slow axis of the QWP ( $\theta$ ) is varied. These

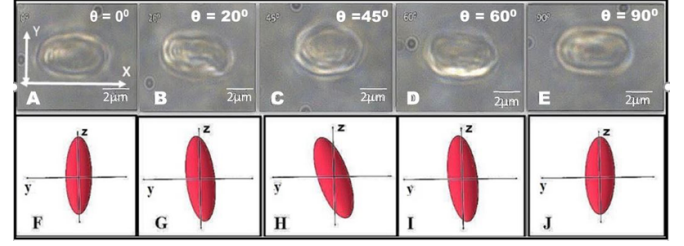


**Figure 5.** Variation in the final position after the second reorientation of cRBC as seen along laser propagation direction for different angles of the quarter-wave plate slow axis (indicated in the left top corner) with respect to the electric field vector of the incident laser beam. Figures (A)–(E) shows the images obtained experimentally viewed in the XY plane of the reference frame and figures (F)–(J) shows the corresponding schematic if viewed from the YZ plane. (Note that the tilt of the major axis could be towards the right as well.)

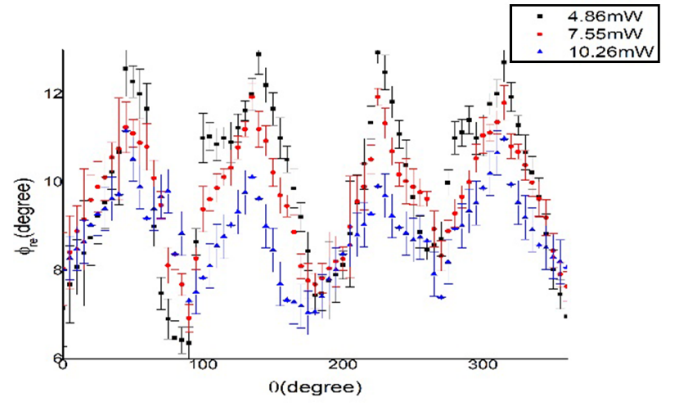


**Figure 6.** Variation of  $\Phi_{\text{re}}$  in the second partial reorientation measured from the projections of the image in a plane perpendicular to the laser propagation direction (Z-axis). The measurement is carried out for three different laser powers at the sample stage.

are images seen along the laser propagation direction, which is the Z-axis of the coordinate system of the laboratory frame. A schematic of the views in the YZ plane for the images in figures 5(A)–(E), are shown in figures 5(F)–(J), for illustrative purposes.

We observe that when a laser beam with elliptical polarization is used, the cell first invariably undergoes a complete 90° reorientation about the major axis and then a second incomplete one about the minor axis. We call the angle subtended by the major axis of the cRBC with the beam propagation direction in this final orientation, as  $\Phi_{\text{re}}$ .  $\Phi_{\text{re}}$  is obtained from the length of the image projected in the XY plane, as seen in figures 5(A)–(E). The minimum value of  $\Phi_{\text{re}}$  occurs for linearly polarized light while the maximum value for  $\Phi_{\text{re}}$  is obtained for circularly polarized light. Appendix C provides details of the calculation of  $\Phi_{\text{re}}$  from the measured length along the Y-axis of the image projected on the focal plane, using image analysis routines.

The variation in  $\Phi_{\text{re}}$  has been measured for different laser powers at the sample stage (4.86 mW, 7.55 mW, and 10.27 mW) as shown in figure 6.  $\Phi_{\text{re}}$  displays the same variability even when the trap stiffness is changing with laser power.



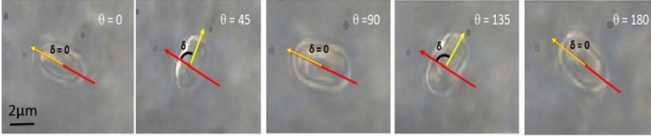


**Figure 7.** Variation in the angle of deviation of the longest transverse of cRBC (after second orientation) ( $\delta$ ) in the XY plane with respect to the orientation at  $\theta = 0^\circ$ . The red marker indicates the orientation with respect to  $\theta = 0$  and the position of the yellow marker indicates the change in the angle  $\delta$  for different values of  $\theta$ . The power at the sample stage for these images is 7.55 mW.

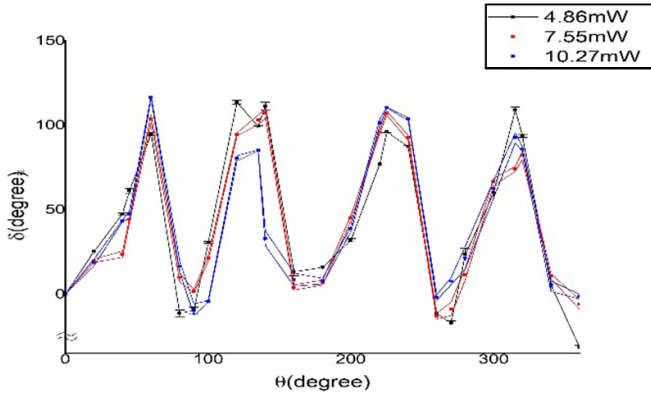


**Figure 8.** Variation of  $\delta$  in the X–Y plane (trapping plane) to the initial orientation at  $\theta = 0^\circ$  for different powers of the laser at the sample stage.

However, the extent of partial orientation is reduced as the power increases. This can be attributed to the increase in the trap stiffness that in turn results in lowering  $\Phi_{re}$  as shown in figure 6. For powers greater than 10.27 mW, we are unable to measure  $\Phi_{re}$  since the variation in the value obtained is within the error bars in our measurements.

We also observe a second type of variation. This is a change in the orientation of the longest transverse in the XY plane (plane of observation) with alterations in  $\theta$ . We call the angle of deviation of this longest transverse with respect to the position of the same at  $\theta = 0^\circ$ , as  $\delta$ . Figure 7 shows the variation of  $\delta$  for different angles of  $\theta$ .

We observe that when the trapping beam is linearly polarized, the orientation of the longest transverse of cRBC after the second orientation is always along the same direction as shown in figure 7(A). As  $\theta$  increases, so does  $\delta$ , with the latter reaching a maximum value when the incident laser beam is circularly polarized. We note further, that the variation in  $\delta$  is similar for different powers at the sample stage, as shown in figure 8.

### 2.3. Model for calculating partial reorientations

We have employed the ray optics approximation for explaining the partial reorientations of cRBCs. For simplicity, we approximate the shape of the cRBC trapped in a Gaussian beam optical tweezer to that of a homogeneous prolate ellipsoid. Though we have considered a non-spherical particle to

describe the trapping dynamics, we may still use the equations of force corresponding to that for a spherical particle if the particle is convex in terms of its morphology [20]. The total force acting on a dielectric sphere due to a single ray of light  $\vec{F}_{ray}$  incident in a medium of refractive index  $n_m$  along an incident vector  $\hat{r}_i$  and power  $P_i$ , is given by

$$\vec{F}_{ray} = \frac{n_m P_i}{c} \hat{u}_i - \frac{n_m P_r^{(1)}}{c} \hat{u}_r - \sum_{j=2}^{\infty} \frac{n_m P_t^{(j)}}{c} \hat{u}_t^{(j)} \quad (6)$$

where  $\hat{u}_i$ ,  $\hat{u}_r$  and  $\hat{u}_t^{(j)}$  are the unit vectors in the direction of the incident ray, the first reflected ray, and the  $j$ th transmitted ray respectively, with corresponding powers being  $P_i$ ,  $P_r^{(1)}$ , and  $P_t^{(j)}$ . This force, when acting on a particle lacking spherical symmetry, leads to a torque [20] given by,

$$\vec{\tau}_{ray} = (\mathbf{P}_1 - C) \frac{n_m P_i}{c} \hat{u}_i - (\mathbf{P}_1 - C) \frac{n_m P_r^{(1)}}{c} \hat{u}_r - \sum_{j=2}^{\infty} (\mathbf{P}_j - C) \frac{n_m P_t^{(j)}}{c} \hat{u}_t^{(j)} \quad (7)$$

where  $C$  is the centre of mass of the trapped particle and  $\mathbf{P}_j$  is the  $j$ th position of the scattering ray with respect to  $C$ . Using equations (6) and (7), we simulate the optical forces and corresponding torques acting on the prolate ellipsoid, keeping all the trapping parameters the same as that in the experiment. We assume that the major axis initially, is nearly perpendicular to the beam propagation direction at time  $t = 0$  and track the orientation angle  $\Phi_{re}$  with respect to the laser propagation direction as a function of time, till the ellipsoid reaches its final stable equilibrium position. The initial angle of orientation at  $t = 0$  is set as  $80^\circ$  with respect to the Z-axis of the lab frame and the angle of orientation is computed every 0.001 s with an angular resolution of  $0.001^\circ$ . Since the orientation is unbiased, the simulations can result in showing the ellipsoid orienting from  $0^\circ$  to  $90^\circ$  or from  $0^\circ$  to  $-90^\circ$ , and therefore, the initial orientation angle is set to  $80^\circ$ .

We image the intensity profiles of the laser beam in the focal plane in our experimental setup for various settings of the QWP and show the variation in intensity along the X and Y axes of the lab frame, in figure 9. While the intensity along the X-axis of the frame remains the same, the intensity along the Y-axis varies as the QWP is rotated as shown in figure 9. We clarify that we have chosen the X-axis in our experiments and simulations, as the axis of constant radial intensity distribution and the Y-axis, as the axis of the variable radial intensity distribution. We have observed in our experiments and simulations that the change in the intensity profile, and hence the electric fields across a trapped microstructure, result in a change in the net torque [21], that causes the observed partial second reorientation.

The general equation of the electric field for Gaussian intensity profiles along the X and Y axes are written as

$$\vec{E}(r) = E_0 e^{-\frac{r^2}{w_0^2}} \hat{r} \quad (8)$$

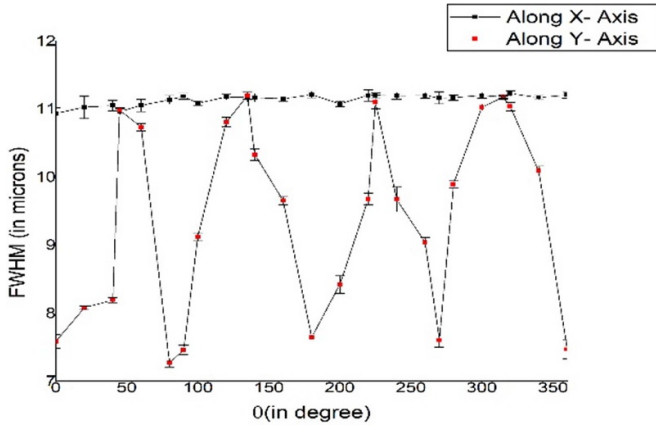


**Figure 9.** Variation in the FWHM of the intensity profile of the laser beam at the focus of the optical trap observed experimentally along the X-axis (in black) and the Y-axis (in red). It is seen that the variation is minimal along the X-axis.

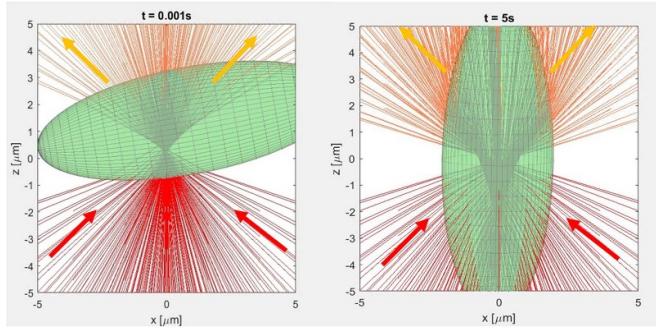


**Figure 10.** Initial and final positions of the major axis of the ellipsoid trapped in a linearly polarized optical trap from simulations. The orange lines in the graphical representation are the incident and scattered light rays coming towards and away respectively from the trapped ellipsoid (in green).

where  $r$  is the radial coordinate,  $w_0$  is beam waist,  $\varepsilon_0$  is the dielectric permittivity of vacuum, and  $E_0$  is the amplitude of the electric field intensity at  $r = 0$ . Simulations have been carried out using the Ray-Optics toolbox developed by Volpe *et al* [20], with a modified electric field distribution along the X and Y axes of the focal region given by equation (8). Figure 10 below is the representation of the dynamic variation of orientations observed in simulations, from a side-view perspective.

Since we have used a model ellipsoid shape to represent the trapped object in the simulation, only the second orientation, i.e. the variation in  $\Phi_{re}$ , can be modelled. The model ellipsoid is cylindrically symmetric, thus precluding any energy minimization principle coming into the picture. Hence in this model, we are restricted to computing the second reorientation.

In figure 11, we show the variation of the instantaneous value of  $\Phi_{re}$  as a function of time in our simulations for linear (red) and circular (black) polarizations. We observe that as  $t$  increases,  $\Phi_{re}$  decreases monotonically and reaches its equilibrium value of  $\Phi_{re} = 0^\circ$ , for the case of linear polarization, and  $\Phi_{re} = 5.41^\circ$  for the case of circular polarization,

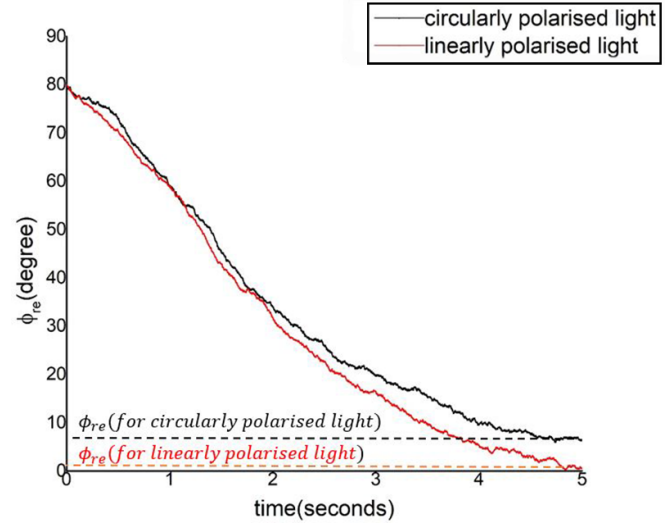


**Figure 11.** Graphical representation of reorientation angle versus time for an ellipsoid trapped using linearly polarized light (red) and (b) circularly polarized light (black).

at a laser power of 4.86 mW. In the simulations, the criterion we employ for deciding when the final equilibrium position is attained for recording any particular  $\Phi_{re}$ , is when the angular variation between two successive values becomes lesser than or equal to the angular resolution limit of  $0.0001^\circ$ , the value that is set in our calculations. We have carried this out for at least 20 iterations. By increasing the number of iterations, we have observed no significant change in the orientation angles that we compute. If the simulations are indeed run for sufficiently longer durations (as long as 10 s), we observe that the reorientation angle gradually turns into a complete reorientation ( $\Phi_{re} = 0$ ) of the ellipsoid irrespective of the polarization of the laser. However, this has not been observed experimentally, even for longer durations of observation. We attribute the possible reasons for this asymptote in the simulations to employing the geometrical ray optics approximation in the analysis, and further, to effects, possibly due to the optical anisotropy of the system. The effects of this optical anisotropy, however, were calculated and found to be very small, and hence not considered in the simulations. Moreover, the simplifying assumption of the shape to be that of a perfect ellipsoid in the simulations, and further, neglecting the actual induced shape variations observed in the cells during the course of the experiment, could all be reasons for the variance between our computation and experiment. Taking  $\vec{E}$  along X-axis as  $E_x$  and along the Y-axis as  $E_y$ , this process is repeated for different values of  $E_y$ . As  $E_y$  increases from 0 to  $E_0$ , so does  $\Phi_{re}$ , gradually, but by a small amount, attaining a maximum value when  $E_x = E_y$ . Thus, we see in figure 11 that while the final equilibrium orientation for the linear polarization is  $0^\circ$ , for the case of circular polarization, it is observed to be  $5.41^\circ$  at low power (4.86 mW).

We note a deviation in the aspect ratios of the intensity profile of the laser beam at the focus in our experiments from that of the theoretically expected value. Although ideally the

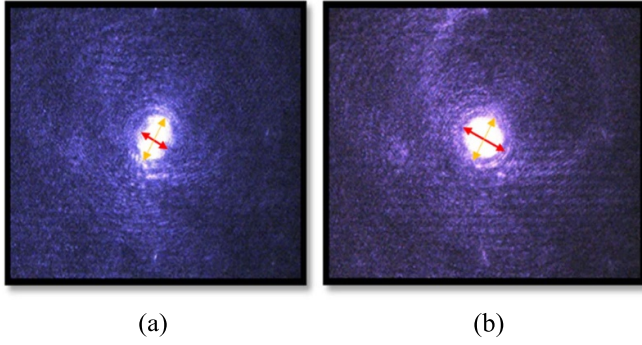


**Figure 12.** Images of intensity profiles of the incident laser beam at the focus of the optical trap for (a) linearly polarized light and (b) for circularly polarized light. It is seen that  $I_x$  remains unaltered but  $I_y$  has slightly decreased. X-axis (in orange) and Y-axis (in red) represent the axis of constant radial intensity distribution and the axis of the variable radial intensity distribution.

value of  $E_y$  and the corresponding beam intensity  $I_y$  is zero for linearly polarized light, the actual value of  $I_y$  is not zero in our experiments. This can play a role in influencing the partial orientations observed. Figure 12 shows images of the laser beam profiles at the focus in the experimental setup, for linear (figure 12(a)) and circularly (figure 12(b)) polarized light. This is due to the polarization effects that are observed at the focus of objectives of high numerical aperture. In such cases, we observe that when linearly polarized light is focused, the intensity that ought to be predominantly along say, the X-axis, gets distributed (albeit by small amounts) along the Y and Z axes [22].

This change in intensity profile affects the experimental  $\Phi_{re}$ . When we calculate the theoretical  $\Phi_{re}$  using the intensity profiles obtained in our experiments, that is with a non-zero value to the intensity spread along Y-axis for linearly polarized light, the theoretical and experimental values of  $\Phi_{re}$  can be seen to be in fair agreement with each other. In fact, we calculated The Pearson correlation coefficient between the  $\Phi_{re}$  and the FWHM of the intensity distribution along the Y-axis is found to be 0.9. It is thus observed that there is a strong correlation between the change in the intensity beam profile to the partial orientations of the cRBCs. The variation of partial orientations of cRBCs obtained through simulations and our experiments are compared and shown below in figure 13.

We note that though the first and second reorientations of cRBC about the major and minor axes respectively, can be attributed to an energy minimization condition, as discussed in section 2.1, the final orientation angle in the first reorientation remains unaltered whereas the final angle in the second reorientation depends significantly on the intensity profile of the laser beam at the focus. This can be substantiated by comparing the variation of partial orientations (figure 6) with that of the intensity along the Y-axis (figure 9) with  $\theta$ . The torque induced due to the (weak) birefringence of the cRBC membrane is acting as a contributing factor only to negate the rotational diffusion of the cell in the trap and does not have a role in determining the final orientation of the cell. We have estimated

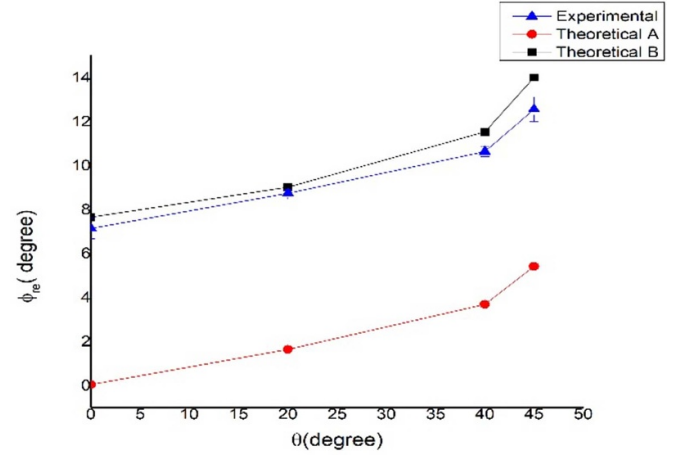


**Figure 13.** Comparison of the orientation angle of cRBCs obtained from experiments (in blue) and through simulations with theoretical aspect ratios (in red) and through simulations with experimental beam intensity profiles (in black) keeping power as 4.86 mW.

the alignment torque that results due to the cell's birefringence [23] using a value that we measured in previous work, for an hRBC [24]. This torque was found to be two orders of magnitude smaller in comparison to the laser-induced torque.

### 3. Conclusions

In this paper, we report the variation in the final equilibrium orientation of cRBCs in a single beam optical tweezer with changing the polarization of light. We observe that when a cRBC is trapped in the OT, two reorientation processes about the major and short minor axes of the cell are required for it to attain its final equilibrium orientation. We justify this process of reorientation under the influence of linearly polarized light, by calculating the work done by optical forces acting on the particle to align the cell along the laser beam direction. Further, we find that the second orientation of cRBC is dependent on the ellipticity in the polarization of the incident laser beam. We calculate the corresponding angles of reorientation  $\Phi_{re}$  for the cells, for different ellipticities in the polarization, and compare our results with the values obtained from simulations. These studies point to the change in the intensity distribution of the laser beam at the trapping plane as the predominant contributing factor to the partial reorientations that we have observed.

Gaining an understanding of optical micromanipulation and orientation of such micro-sized objects is essential for developing efficient non-invasive tools in studying inter and intracellular processes. These studies have relevance in the design of micro-machines that can perform controlled rotational motion and orientation at small length scales. Most of the experiments performed have previously focused on using non-biological birefringent micro-objects. While having advantages, in terms of stability and durability in their performance, many of them lack compatibility with biological specimens when used for *in vivo* studies. The possibility of



using naturally occurring biological shapes as biocompatible tools for such studies can be relevant in this context.

### Data availability statement

The data that support the findings of this study are available upon reasonable request from the authors.

### Acknowledgments

The authors acknowledge Dr Veere Gowda for providing the avian blood samples and for useful discussions. They also thank Ms Shruthi. S Iyengar for assistance in the experiment and useful discussions, Dr Amey Joshi, for suggestions related to the simulations, and Ms Ashwini. V Bhat for assistance in the imaging of beam profiles. One of the authors (CD) acknowledges the Department of Science and Technology (DST) for financial assistance through the Women in Science fellowship (WOS-A).

### Appendix A. Bending deformation energy calculation for cRBC

We calculate the energy required to bend the cRBC using the Helfrich equation [25]

$$\text{Energy} = \int E_b (2H - C_0)^2 dA$$

where  $H$  is the local curvature,  $C_0$  is the spontaneous curvature and  $E_b$  is the bending modulus.  $H = \frac{C_0 + C_1}{2}$ ; with  $C_1$  being the surface curvature in the perpendicular direction. Assuming that there is no spontaneous curvature, the bending term  $(2H - C_0)^2$  in the energy required can be considered as  $(2H)^2$ . Further, we take the RBC bending modulus as  $E_b = 2 \times 10^{-19} \text{ N m}^{-2}$ , as reported in [26].

Let us consider the cRBC as an ellipse with  $OA$  being the semi-major axis and  $OB$  being the semi-long minor axis, as shown in the figure below. Let us consider the cRBC bending as shown in figure 14(b).

Then  $OA = a = 6 \mu\text{m}$ ;  $OB = b = 4 \mu\text{m}$ ;  $f = \frac{OF}{OA}$ .

Then, the radius of curvature of the bent part of the cRBC ( $F'F$ ),  $r = \frac{fa}{\pi}$ ; Curvature =  $\frac{1}{r}$ ;  $H = \frac{\pi}{2fa}$ . Carrying out the integration only over the shaded region in the ellipse (figure 14(a)) where the curvature is non-zero, we get

$$\begin{aligned} \text{Energy} &= E_b \left( \frac{\pi}{fa} \right)^2 \int dA = E_b \left( \frac{\pi}{fa} \right)^2 \\ &\times \left[ ab \left( 2\sin^{-1}f + \sqrt{1-f^2} \right) \right]. \end{aligned}$$

Figure 15 below shows the energy variation with respect to ' $f$ '. We find that the minimum value of bending energy is  $4.1342 \times 10^{-18} \text{ J}$ .

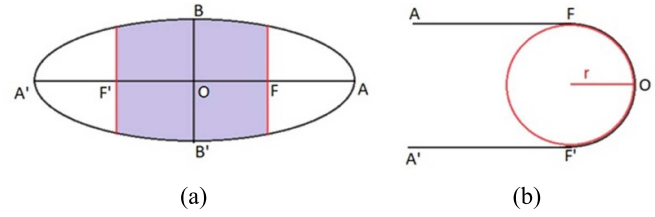


**Figure 14.** (a) Schematic of the cRBC ellipsoid as viewed from above ( $A'A$  is the major axis while  $B'B$  is the long minor axis). (b) Axis  $A'A$  of the bent cRBC as viewed from the side. Note that  $F'$  and  $F$  mark positions beyond which there is no curvature of the membrane.

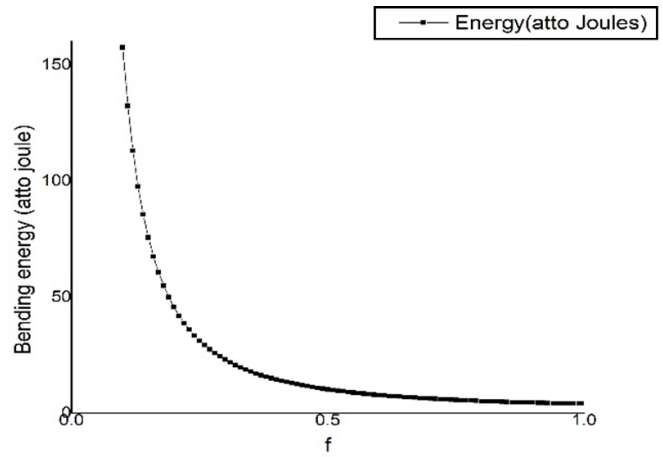


**Figure 15.** Plot of bending energy required with respect to the bending curvature.

### Appendix B. Calculation of inertial torque acting on cRBCs

The schematic for the model considered to calculate the inertial torque of the cRBC is as shown in figure 16. We have considered a model wherein the cRBC is taken to be a combination of a sphere and a disc of uniform density. The dimensions of the cRBC are actual dimensions, as mentioned in [13].

For the model considered above, the moment of inertia  $I_{\text{RBC}}$  is written as

$$I_{\text{RBC}} = I_{\text{sphere}} + I_{\text{disc}}$$

where the moment of inertia for the sphere is given by  $I_{\text{sphere}} = \frac{2}{5}m_{\text{sphere}}r^2$  and the moment of inertia for a uniform disc is given by  $I_{\text{disc}} = \frac{1}{4}m_{\text{disc}}R^2$ .

Therefore, we have,

$$I_{\text{RBC}} = \frac{2}{5}m_{\text{sphere}}r^2 + \frac{1}{4}m_{\text{disc}}R^2.$$

Taking the density of the disc as  $1.139 \times 10^3 \text{ kg m}^{-3}$  from [27] and assuming that the nucleus is  $10^2$  times denser than the cell, we get

$$I_{\text{RBC}} = \frac{2}{5}\rho_{\text{sphere}}(V_{\text{sphere}})r^2 + \frac{1}{4}\rho_{\text{disc}}(V_{\text{disc}})R^2$$

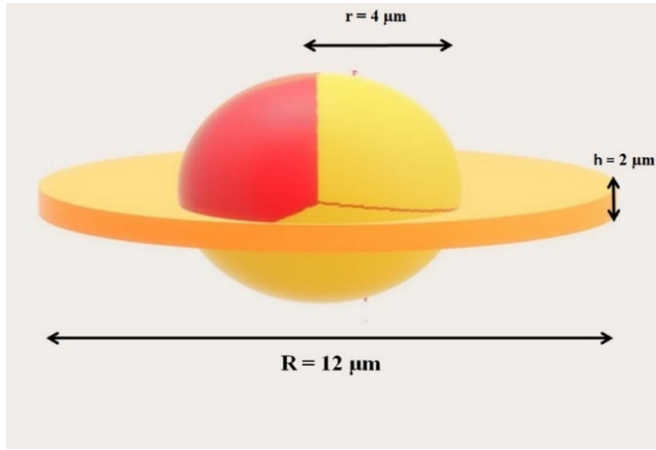


**Figure 16.** Schematic for cRBC model taken for calculation of inertial torque.

where  $V_{\text{sphere}} = \frac{4}{3}\pi r^3$  and  $V_{\text{disc}} = \pi r^2 h$  respectively. Substituting all the values we get,  $I = 1.22 \times 10^{-24}$  kg m<sup>2</sup>. The rotational kinetic energy of the cRBC, the amount of energy required to rotate the cell is given by

$$U_{\text{inertia}} = \frac{1}{2} I \omega^2 \quad (\text{B1})$$

but from equation (1),

$$U_{\text{inertia}} = \tau_{\text{inertia}} \Phi_{\text{re}}. \quad (\text{B2})$$

Equating (B1) and (B2) and considering the experimental observations, where we observe that a cRBC reorients through an angle of  $\Phi_{\text{re}} = 90^\circ$  in  $t = 0.25$  s, we obtain  $U_{\text{inertia}} = 24.09 \times 10^{-22}$  J and  $\tau_{\text{inertia}} = 15.33 \times 10^{-22}$  Nm which is four orders of magnitude smaller than the laser-induced torque. Therefore, we consider the contribution of the corresponding inertial torque to be zero in our calculations.

### Appendix C. Determination of reorientation angle $\Phi_{\text{re}}$ using the edge detection method

To calculate the angle of orientation of cRBCs with respect to the laser propagation direction, we record videos of the entire reorientation process using a CCD camera with the image taken on the plane perpendicular to the laser propagation direction (XY plane). Images are extracted from these videos to be analysed using ImageJ software and taken such that the cell is viewed along the Z-Axis (or viewpoint as mentioned in figure 14 below). Using the edge detection method, we measure the projected lengths of the width of the cell in the image. When the cRBC is aligned completely along the laser beam, the projected length of the width of the cRBC is just the short minor axis of the cRBC (i.e.  $t = 4 \mu\text{m}$ ). When the ellipticity of the polarization changes, then the projected length increases gradually as illustrated in figure 17.

Let the cell be represented by a rectangle where  $R$  is the radius and  $t$  is the thickness of cRBC in this figure, which is orienting itself along the laser beam direction (Z-axis). If the

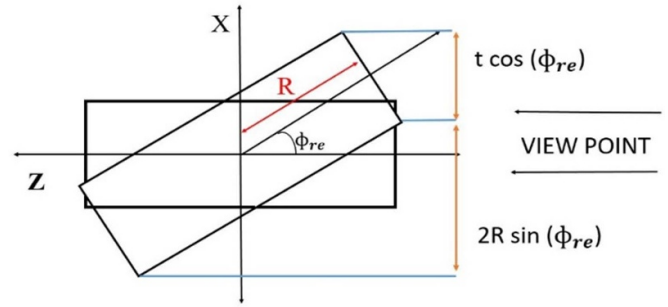


**Figure 17.** A pictorial representation of edge detection technique to measure the orientation angle  $\Phi$ .

final reorientation angle is  $\Phi_{\text{re}}$  after the cell reaches a stable equilibrium, by geometry, we obtain the projected length on the image plane (X–Y plane) as

$$h = 2R \sin \Phi_{\text{re}} + t \cos \Phi_{\text{re}}$$

solving for  $\Phi_{\text{re}}$ , we obtain the value of  $\Phi_{\text{re}}$ , as

$$\Phi_{\text{re}} = \sin^{-1} \frac{h}{\sqrt{(4R^2 + t^2)}} - \sin^{-1} \frac{t}{\sqrt{(4R^2 + t^2)}}.$$

### ORCID iDs

Chetana D  <https://orcid.org/0000-0002-4263-3098>

Sharath Ananthamurthy  <https://orcid.org/0000-0002-3112-5995>

### References

- [1] Cheng Z, Chaikin P M and Mason T G 2002 Light streak tracking of optically trapped thin microdisks *Phys. Rev. Lett.* **89** 108303
- [2] Dasgupta R, Ahlawat S and Gupta P K 2007 Trapping of micron-sized objects at a liquid-air interface *J. Opt. A* **9** S189
- [3] Gauthier R C 1997 Theoretical investigation of the optical trapping force and torque on cylindrical micro-objects *J. Opt. Soc. Am. B* **14** 3323–33
- [4] Gauthier R C, Ashman M and Grover C P 1999 Experimental confirmation of the optical-trapping properties of cylindrical objects *Appl. Opt.* **38** 4861–9
- [5] Cao Y, Stilgoe A B, Chen L, Nieminen T A and Rubinsztein-Dunlop H 2012 Equilibrium orientations and positions of non-spherical particles in optical traps *Opt. Express* **20** 12987–96
- [6] Wulff K D, Cole D G and Clark R L 2008 Controlled rotation of birefringent particles in an optical trap *Appl. Opt.* **47** 6428–33
- [7] Sheu F-W, Lan T-K, Lin Y-C, Chen S and Ay C 2010 Stable trapping and manually controlled rotation of an asymmetric or birefringent microparticle using dual-mode split-beam optical tweezers *Opt. Express* **18** 14724–9
- [8] Friesen M E J, Nieminen T A, Heckenberg N R and Rubinsztein-Dunlop H 1998 Optical torque controlled by elliptical polarization *Opt. Lett.* **23** 1–3
- [9] Friesen M E J, Nieminen T A, Heckenberg N R and Rubinsztein-Dunlop H 1998 Optical alignment and spinning of laser-trapped microscopic particles *Nature* **394** 348–50

- [10] Dharmadhikari J A, Roy S, Dharmadhikari A K, Sharma S and Mathur D 2004 Naturally occurring, optically driven, cellular rotor *Appl. Phys. Lett.* **85** 6048–50
- [11] Rothmayer M, Tierney D, Frins E, Dultz W and Schmitzer H 2009 Irregular spin angular momentum transfer from light to small birefringent particles *Phys. Rev. A* **80** 043801
- [12] Search bionumbers—the database of useful biological numbers (harvard.edu) (available at: <https://bionumbers.hms.harvard.edu/search.aspx?task=searchbytrmorg&log=y&trm=Chicken%20Gallus%20gallus>)
- [13] Chetana D et al 2020 Reorientation dynamics and micromanipulation of natural microscopic soft matter in an optical trap with varying polarization of the laser *AIP Conf. Proc.* **2265** 2
- [14] Stout A L and Webb W W 1997 Optical force microscopy *Methods Cell Biol.* **55** 99–116
- [15] Faucheux L P and Libchaber A J 1994 Confined Brownian motion *Phys. Rev. E* **49** 5158
- [16] Neuman K C and Block S M 2004 Optical trapping *Rev. Sci. Instrum.* **75** 2787–809
- [17] Parthasarathi P, Nagesh B V, Lakkegowda Y, Lyengar S S, Ananthamurthy S and Bhattacharya S 2013 Orientational dynamics of human red blood cells in an optical trap *J. Biomed. Opt.* **18** 025001
- [18] Ghosh A, Sinha S, Dharmadhikari J A, Roy S, Dharmadhikari A K, Samuel J, Sharma S and Mathur D 2006 Euler buckling-induced folding and rotation of red blood cells in an optical trap *Phys. Biol.* **3** 67
- [19] Berg H C 2018 *Random Walks in Biology* (Princeton, NJ: Princeton University Press) p 84
- [20] Callegari A, Mijalkov M, Gököz A B and Volpe G 2015 Computational toolbox for optical tweezers in geometrical optics *J. Opt. Soc. Am. B* **32** B11–B19
- [21] Khan M, Mohanty S K and Sood A K 2005 Optically-driven red blood cell rotor in linearly polarized laser tweezers *Pramana* **65** 777–86
- [22] Mansuripur M 1986 Distribution of light at and near the focus of high-numerical-aperture objectives *J. Opt. Soc. Am. A* **3** 2086–93
- [23] Higurashi E, Sawada R and Ito T 1999 Optically induced angular alignment of trapped birefringent micro-objects by linearly polarized light *Phys. Rev. E* **59** 3676
- [24] Nagesh B V et al 2014 Birefringence of a normal human red blood cell and related optomechanics in an optical trap *J. Biomed. Opt.* **19** 115004
- [25] Selvan R, Parthasarathi P, Iyengar S S, Ananthamurthy S and Bhattacharya S 2019 Estimation of membrane bending modulus of stiffness tuned human red blood cells from micropore filtration studies *PLoS One* **14** e0226640
- [26] Tomaiuolo G 2014 Biomechanical properties of red blood cells in health and disease towards microfluidics *Biomeicrofluidics* **8** 051501
- [27] Godin M, Bryan A K, Burg T P, Babcock K and Manalis S R 2007 Measuring the mass, density, and size of particles and cells using a suspended microchannel resonator *Appl. Phys. Lett.* **91** 123121
- [28] Ortega A and García de la Torre J 2003 Hydrodynamic properties of rodlike and disklike particles in dilute solution *J. Chem. Phys.* **119** 9914–9